Full Particle Simulation of Whistler-Mode Triggered Falling-Tone Emissions in the Magnetosphere

Takeshi Nogi[1] (ID), **Satoko Nakamura[1]** (ID), **and Yoshiharu Omura[1]** (ID)

[1]Research Institute for Sustainable Humanosphere, Kyoto University, Kyoto, Japan

Abstract We perform a one-dimensional electromagnetic full particle simulation for triggered falling-tone emissions in the Earth's magnetosphere. The equatorial region of the magnetosphere is modeled with a parabolic magnetic field approximation. The short whistler-mode waves with a large amplitude are excited and propagate poleward from an artificial current oscillating with a constant frequency and amplitude. Following the excited waves, clear emissions are triggered with a falling frequency. Without the inhomogeneity of the background magnetic field, no triggered emission appears. The falling tone has several subpackets of amplitude and decreases the frequency in a stepwise manner. The positive resonant current formed by resonant electrons in the direction of the wave magnetic field clearly shows that an electron hill is formed in the phase space and causes the frequency decrease. The entrapping of the resonant electrons at the front of the packets and the decrease of the amplitude at the end of packets are essential for the generation of falling-tone emissions. Each wavefront of the emission has a strongly negative resonant current $-J_E$, which results in the wave growth. In the formation process of the resonant currents, we investigate the inhomogeneous factor S, which controls the nonlinear motion of the resonant electrons interacting with waves. The factor S consists of two terms, a frequency sweep rate and a gradient of the background magnetic field. The resonant current J_E in the wave packet changes its sign from negative to positive as the packet moves away from the equator, terminating the wave growth.

1. Introduction

Very low frequency (VLF) chorus emission is one of the most significant wave phenomena in the Earth's magnetosphere. Chorus is commonly observed in the inner magnetosphere as intense whistler-mode waves, in the frequency range of 0.1–0.8 f_{ce} (f_{ce} is the equatorial electron gyrofrequency), with right-hand polarization and propagating along the ambient magnetic field line (e.g., Gurnett et al., 2001; Koons & Roeder, 1990; Meredith et al., 2001; Oliven & Gurnett, 1968; Tsurutani & Smith, 1974, and others). They are composed of coherent wave packets with rising or falling frequency. The artificially excited rising and falling tones have also been observed from weak and monochromatic whistler wave signals, known as "triggered VLF emissions" (Helliwell, 1983; Helliwell & Brice, 1964; Helliwell & Katsufrakis, 1974; Helliwell et al., 1980, 1986). Comparisons between chorus emissions and triggered emissions have revealed that the triggered emissions have the same generation mechanism as chorus (Helliwell, 1988; Nunn, 1986, 1990; Trakhtengerts et al., 1996).

In general, the source of whistler-mode waves is associated with anisotropic energetic electrons in the equatorial region (Kennel & Petschek, 1966; LeDocq et al., 1998; Parrot et al., 2003; Santolík et al., 2004, 2005, 2008; Tsurutani & Smith, 1974; Tsurutani et al., 1979). It has been explained by both linear and quasi-linear theory (e.g., Cornilleau-Wehrlin et al., 1985; Hashimoto & Kimura, 1981; Solomon et al., 1988, and others). On the other hand, in the generation of the discrete structure of chorus, nonlinear processes play an important role. In the nonlinear growth theory, the resonant current formed by electron trapping results in the rapid growth of amplitude and the time variation of rising and falling frequencies (Nunn et al., 1997, 2009; Omura et al., 2008, 2009).

For a better understanding of these complicated nonlinear processes, many numerical simulations have been conducted, reproducing nonlinear trapping of resonant electrons. A one-dimensional Vlasov hybrid code has been developed for simulating chorus emissions (Nunn, 1974). Nunn and Omura (2012) have shown that a falling-tone emission can be excited from the upstream region by a triggering pulse with a constant frequency. Katoh and Omura (2007) and Tao (2014) have successfully reproduced rising tones by
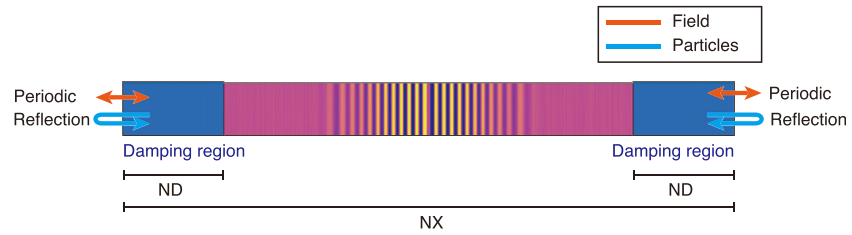
Figure 1. The schematic illustration of the one-dimensional simulation model. Total simulation region (NX) includes damping region (ND).

self-consistent electron hybrid codes, assuming energetic electrons with a temperature anisotropy. Hikishima et al. (2010) have developed a full-particle simulation for chorus and triggered emissions. As for the background magnetic field model, Ke et al. (2017) have expanded the electron hybrid codes from 1-D to 2-D model and also reproduced discrete rising-tone emissions. Recently, Lu et al. (2019) have reported a 2-D simulation of rising-tone emissions in the dipole magnetic field.

In this paper, we conduct a one-dimensional self-consistent full particle-in-cell (PIC) calculation for simulating a triggered falling-tone emission. Section 2 describes the simulation model, initial conditions, and the method of triggering whistler-mode waves. In section 3, we show the results of exciting a triggered falling-tone emission. We discuss the generation process of the emission based on the dynamics of resonant currents in section 4. Finally, section 5 gives the conclusions.

2. Simulation Model

To simulate triggered chorus emissions, we use a one-dimensional full PIC code, which is developed from Kyoto University ElectroMagnetic Plasma cOde (KEMPO) by Omura and Matsumoto (1993) and Omura (2007). We adopt a cylindrical coordinate with the x axis along the nonuniform magnetic field. The background magnetic field is assumed axisymmetric and parabolic as a function of x. One-dimensional Maxwell's equations and three-dimensional equations of motion are solved for transverse electromagnetic fields and electrons, respectively. We assume an ideal situation of triggered emissions, which are excited from an artificial signal at the magnetic equator. The simulation system is illustrated in Figure 1.

2.1. Simulation Box

The simulation requires boundary conditions for both particles and electromagnetic fields. Energetic particles are reflected at the edge of the simulation box conserving the adiabatic momentum and randomizing the gyration phase. For electromagnetic fields, we couple the periodic condition and the absorbing boundary condition developed by Umeda et al. (2001). The first and last arrays of the grid are treated with periodic conditions, and the damping region suppresses the amplitude and retards the phase of the outgoing waves.

2.2. The Background Magnetic Field

We set the x axis along the field line. Near the magnetic equator, the x component of the dipole magnetic field B_x is approximated by parabolic variation as

$$B_x(x) = B_{eq}(1 + ax^2),\qquad(1)$$

where x is the distance along the field line from the equator, and B_{eq} and a are the equatorial value of B_x and the coefficient of the parabolic variaton of the background magnetic field, respectively.

To solve the motion of electrons gyrating around the x axis in the above parabolic magnetic field, the radial component of the magnetic field B_r must be taken into account to satisfy $\nabla \cdot \boldsymbol{B} = 0$. The radial magnetic field B_r is given by
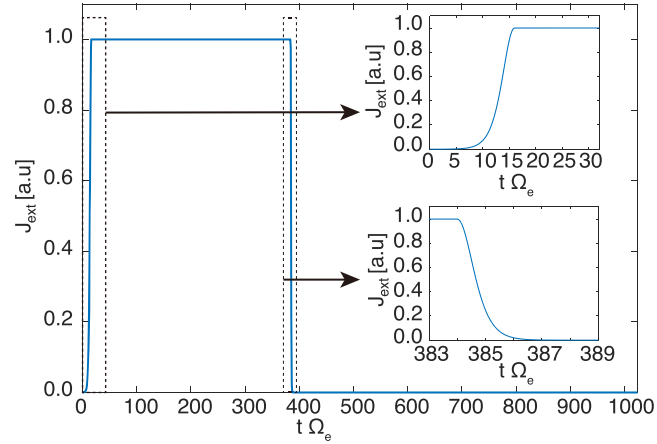
Figure 2. The time profile of the magnitude of injecting currents.

$$B_r = -\frac{\rho_c}{2}\frac{\partial B_x}{\partial x},\tag{2}$$

where ρ_c is the cyclotron radius of an electron.

Substituting Equation 1 to Equation 2, we have the vectors of the radial magnetic field for an individual super particle by

$$\boldsymbol{B_r} = \frac{m_0\gamma(\boldsymbol{v}_\perp \times \boldsymbol{e_x})ax}{-e(1+ax^2)},\tag{3}$$

where $\boldsymbol{e_x}$, $\gamma = \dfrac{1}{\sqrt{1-(v/c)^2}}$, and $\boldsymbol{v}_\perp$ are unit vector parallel to the ambient magnetic field, Lorentz factor, and perpendicular velocity, respectively. The electron charge and rest mass are given by $-e$ and m_0, respectively.

2.3. Initialization of Particle Distribution

The model consists of three species of particles: cold electrons, cold protons, and energetic electrons. Thermal electrons and protons have a bi-Maxwellian distribution, while energetic electrons have a subtracted-Maxwellian distribution. For a marginally stable condition in the region, we define the initial velocity distribution of energetic electrons as follows.

Using the relativistic momentum $u_\parallel = \gamma v_\parallel$ and $u_\perp = \gamma v_\perp$ (the parallel and perpendicular components to the background magnetic field), we define the velocity distribution function of enegetic electrons at the equator f_{eq} as

$$f_{eq}\left(u_{\parallel eq},\, u_{\perp eq}\right) = C_N \exp\left(-\frac{u_{\parallel eq}^2}{2U_{t\parallel}^2}\right)g_{eq}\left(u_{\perp eq}\right)H\left(\arctan\left(\frac{|u_{\perp eq}|}{|u_{\parallel eq}|}\right)-\alpha_{\text{loss}}\right),\tag{4}$$

$$g_{eq}\left(u_{\perp eq}\right) = \frac{1}{1-\beta}\left\{\exp\left(-\frac{u_{\perp eq}^2}{2U_{t\perp}^2}\right)-\exp\left(-\frac{u_{\perp eq}^2}{2\beta U_{t\perp}^2}\right)\right\},\tag{5}$$

where C_N is a normalization coefficient for the distribution function, $H(x)$ is a Heviside step function, α_{loss} is a losscone angle, β is a subtraction ratio. The Heviside function is used to completely elimitnate electrons in the loss cone. Using the velocity distribution function at the equator, each superparticle is distributed from the magnetic equator to the mirror point with conservation of a magnetic momentum and kinetic energy. Charged particles travel with harmonic bounce oscillations along the parabolic magnetic field. The position x and the momentum in the off-equatorial region $(u_\parallel, u_\perp)$ are given from the uniformly distributed phase ϕ as

Table 1
Simulation Parameters for Each Case

Parameter	Case 1	Case 2	Case 3
Coefficient of parabolic magnetic field $a\,c^2\Omega_e^{-2}$	4.48×10^{-5}	4.48×10^{-5}	Uniform
Frequencies of triggering wave (constant) ω	$0.3\,\Omega_e$	$0.51\,\Omega_e$	$0.51\,\Omega_e$

$$x = x_m \cos\phi \ (0 \leq \phi < 2\pi), \tag{6}$$

$$u_\perp = u_{\perp eq}\sqrt{1 + ax^2}, \tag{7}$$

$$u_\parallel = u_{\parallel eq}\sqrt{1 - (u_{\perp eq}/u_{\parallel eq})^2 ax^2}, \tag{8}$$

where x_m is the distance from the magnetic equator to the magnetic mirror point.

2.4. Triggering Waves for Chorus Emissions

At the equator, we put an external sinusoidal current J_z oscillating with a constant frequency for a finite time duration. Basically J_z generates E_z variations around the equator. The excited field propagates as whistler-mode wave packets with a circular polarization in y and z as they move away from the equator. The external current J_z has nothing to do with resonant currents, which will be described in section 4. To reduce the Gibbs oscillation noise from the onset and the termination of the current, the window function is applied as $\cosh(t - \Delta t)$, where $\Delta t = 15\,\Omega_e^{-1}$ and $384\,\Omega_e^{-1}$ at the begining and the end of the triggering, respectively. Figure 2 shows the time evolution of the magnitude of the external current.

2.5. Simulation Parameters

In this paper, we report three different cases, as shown in Table 1. In the present paper, we compare Cases 1 and 2 to survey the generation mechanisms for different frequencies. Case 3 represents a uniform magnetic field model to compare with the effect of the parabolic background magnetic field model. In the present paper, we set the frequency as $0.51\,\Omega_e$ so that the group velocity and the phase velocity of whistler-mode waves take the same value at a certain distance from the equator. Table 2 shows numerical and plasma parameters in the simulations, normalized by the speed of light c in a vacuum and the electron cyclotron frequency Ω_e at the magnetic equator.

Table 2
Common Simulation Parameters in All Cases

| Parameter	Value
Time step	$0.007812\,\Omega_e^{-1}$
Grid spacing	$0.025\,c\Omega_e^{-1}$
Number of grids (NX)	8,192
Length of simulation region	$204.8\,c\Omega_e^{-1}$
Total number of cold electrons N_c	2,147,483,648
Total number of energetic electrons N_h	2,147,483,648
Total number of protons N_i	268,435,456
Mass ratio of proton to electrons m_i/m_e	1,600
The avarage plasma frequency of cold electrons ω_{pe}	$2.0\,\Omega_e$
Density ratio of energetic electrons to cold electrons n_h/n_c	0.02
Thermal momenta of energetic electrons at the equator $U_{t\parallel}, U_{t\perp}$	$0.225\,c, 0.250\,c$
Temperature anisotropy $A = T_\perp/T_\parallel - 1$	0.235
Loss cone angle α_{loss}(degrees)	5
Loss cone parameter β in Equation 5	0.09
Amplitude of triggering wave at the magnetic equator (constant) B_w	$0.02\,B_{eq.}$
Number of grids for damping region (ND)	256
Length for damping region	$6.4\,c\Omega_e^{-1}$
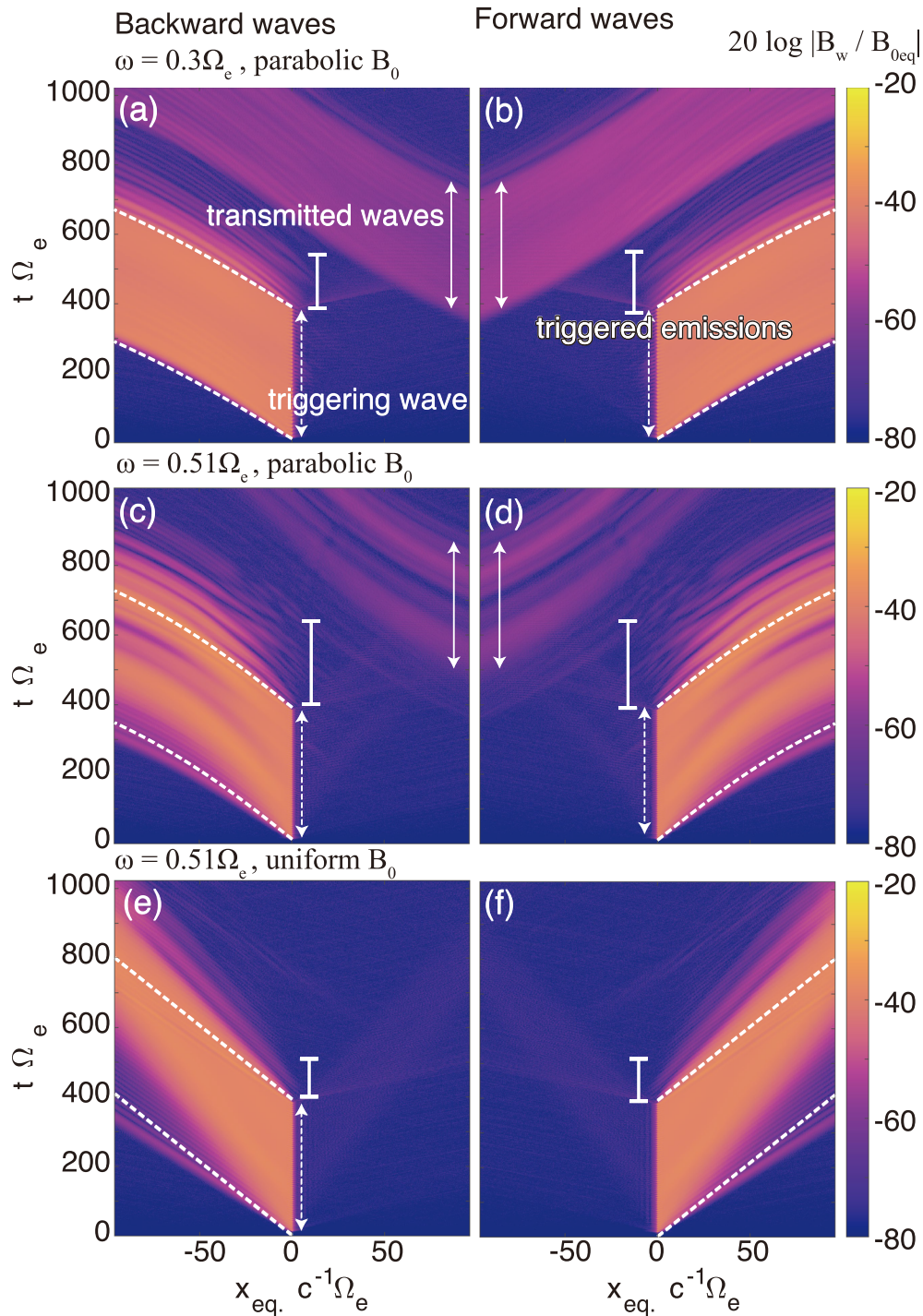
Figure 3. Spatial and time profiles of magnetic field magnitude for forward and backward waves with the frequencies of (a, b) $\omega = 0.3\Omega_e$ and (c-f) $0.51\,\Omega_e$. White dashed lines show head and tail of the triggering wave, calculated as the waves with the triggering frequency that propagates with the group velocity given by the local cold plasma dispersion relation.

3. Simulation Results

3.1. Wave Propagation

We first show wave power profiles in space and time. Figures 3a-b and 3c-f show magnetic field powers with the frequencies of $\omega = 0.3\Omega_e$ and $0.51\,\Omega_e$, respectively. For comparison, Figures 3e and 3f present the case with a uniform background magnetic field.

In all cases, triggering waves are excited from $t = 40\,\Omega_e^{-1}$ to $384\,\Omega_e^{-1}$, and propagate forward (northward) and backward (southward) in the x direction. We separate forward and backward components of parallel-propagating whistler-mode waves by means of the spatial helicity along the background magnetic field. The backward waves and forward waves show symmetric results, and we focus on the forward waves in this paper.

After the stop of triggering, several subpackets are triggered. The triggered emissions appear during 400–600 Ω_e^{-1}, $700\,\Omega_e^{-1}$, and $500\,\Omega_e^{-1}$ in Figures 3b, 3d, and 3f, respectively. We observe that significant wave damping takes place at the wavefront for $\omega = 0.51\,\Omega_e$ for Figures 3d and 3f.

During $t = 400$–$700\,\Omega_e^{-1}$, weak waves are transmitted from the opposite boundary due to insufficient wave damping in the absorbing region. Those transmitted waves do not affect the physical process of our target of triggered emissions, because it is second-order smaller and spatially separated from the main emissions.

3.2. Frequency Analysis on Triggering and Triggered Waves

Figure 4 shows dynamic spectra of transverse magnetic field B_z at different locations along a magnetic field line $x = 20\,c\Omega_e^{-1}$ and $60\,c\Omega_e^{-1}$. The short time fast Fourier transformation is applied over the magnetic field B_z with the Hamming window of 1/8 of total simulation time-shifting in 1/2048 of simulation time. The triggering waves are indicated by solid green lines. Instantaneous frequencies of emissions are overplotted by dashed white lines. We define the emissions by the amplitude greater than 0.3% of B_0 and the coherence between B_y and B_z greater than 0.995. In all cases, we can see a broadband signal at the end of the triggering waves. The signal comes from the artificial termination of the injected current.

After the triggering wave with a constant frequency, triggered emissions can be seen with a small amplitude and a slightly rising frequency in Figures 4a and 4b. In Figure 4c, the triggered emission appears during the period from $t = 500\,\Omega_e^{-1}$ to $600\,\Omega_e^{-1}$. The frequency significantly decreases from $0.51\,\Omega_e$ to $0.3\,\Omega_e$. Figure 4c shows that the duration, amplitude, and frequency drop increase with the propagation. The triggered emission consists of rapid frequency modulation with a time scale of $50\,\Omega_e^{-1}$. Figures 4e and 4f show that there occurs no significant emission in the uniform magnetic field model. There is no significant difference between Figures 4a and 4b and Figures 4e and 4f, whereas Figures 4c and 4d show a significant evolution of the falling-tone emission in space and time. Figure 4 clearly presents that there is neither intense wave growth nor frequency variation in the two cases with $\omega = 0.3\,\Omega_e$ and uniform magnetic field.

We also verify the frequency modulations by examining the time evolution of the electron velocity distribution. The waves should modulate the electron distribution with the resonance velocity determined by the local frequency. Figure 5 shows local velocity distributions of energetic electrons in the $(v_\parallel\text{-}v_\perp)$ plane at respective times and different frequencies of the triggering waves. The blue and green lines in Figure 5 show the cyclotron resonance conditions for the initial and final frequencies of emissions, respectively ($0.3\,\Omega_e$ and $0.35\,\Omega_e$ in Figure 5a, $0.35\,\Omega_e$ and $0.51\,\Omega_e$ in Figure 5b, and $0.51\,\Omega_e$ and $0.54\,\Omega_e$ in Figure 5c). On the resonance curve, the majority of energetic electrons are scattered to lower pitch angles. Figure 5b shows the largest variation of resonance curve, and the most effective scattering along the curves. The green solid lines show the resonance velocity of triggering waves with $0.3\,\Omega_e$ and $0.51\,\Omega_e$, respectively, showing the part of the distribution function scattered by the falling tone. The absolute value of resonance velocity of $0.51\,\Omega_e$ is smaller than that of $0.3\,\Omega_e$. The blue solid and dashed lines show the resonance velocity with $0.35\,\Omega_e$ and $0.54\,\Omega_e$, respectively.

At $t = 200\,\Omega_e^{-1}$, the particle flux increases near the loss cone and decreases at the higher pitch angle on the resonance velocity curve. After that, Figure 5a shows no significant time evolution of the particle distribution. On the other hand, Figure 5b shows gradual modulation of the velocity distribution in a wider area of the velocity phase space. The parallel velocity range of the modulated part of the velocity distribution is shifted to larger absolute values, which corresponds to the decrease of the frequency of the emission. In addition, we can see the enhancement of higher pitch angle particles. Corresponding to the variation range of the resonance curve, there are a greater number of electrons scattered or energized in Figure 5b than in Figures 5a and 5c.
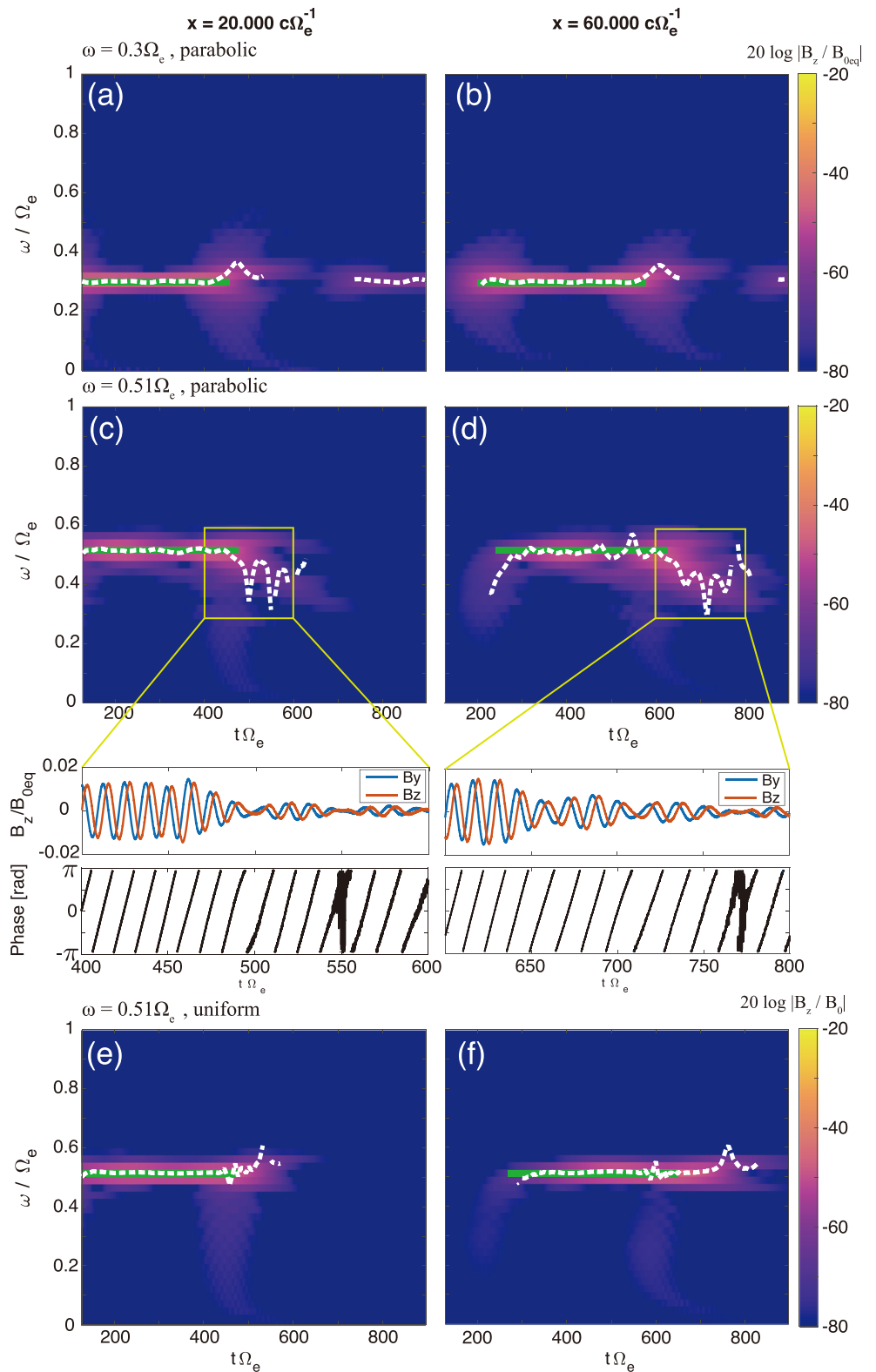
Figure 4. Dynamic spectra of magnetic field magnitude for forward waves with different wave frequencies: (a, b) 0.3 Ω_e and (c–f) 0.51 Ω_e and different background field models: (a–d) parabolic and (e, f) uniform.
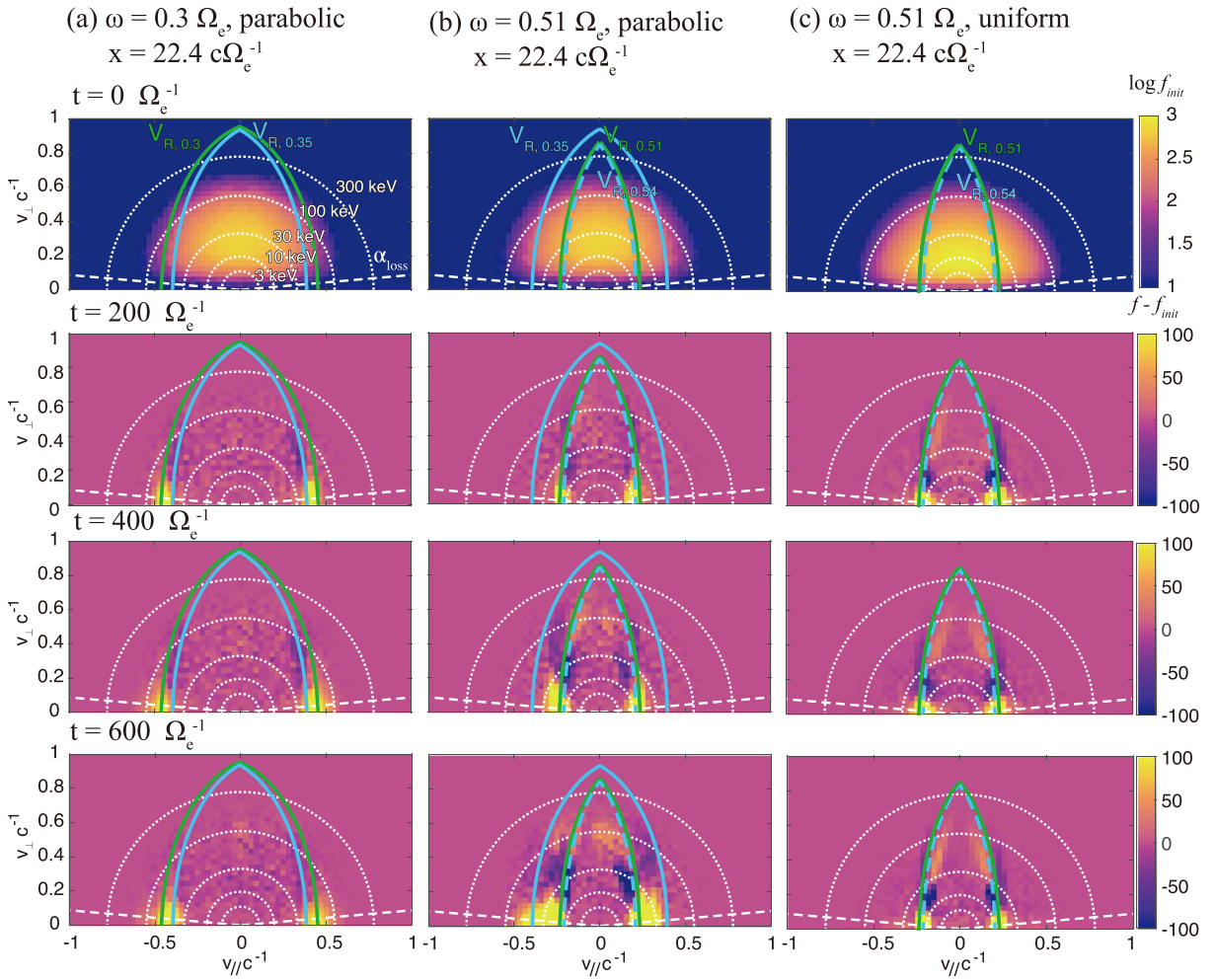
Figure 5. Time evolution of velocity distributions for runs with triggering wave of frequencies (a) $\omega = 0.3\,\Omega_e$ and (b, c) $\omega = 0.51\,\Omega_e$ at $x = 22.4\,c\Omega_e^{-1}$. The white dashed lines indicate the equatorial loss cone angle (5°).

We can see enhanced populations at higher pitch angles in Figure 5b, which indicate a part of electrons are transported to higher pitch angles by nonlinear resonant trapping. Without a gradient of the ambient magnetic field and a frequency variation, the trapped electrons form a symmetric hill in phase space. A symmetric hill cannot cause wave growth. Comparing Figures 5a and 5b, we find that more trapped electrons are energized to higher pitch angles in the falling-tone case. Because of the broadening of the resonance velocity due to the frequency variation, the wave can interact with more particles. The trapped electrons are strongly relating to the electron hill, which induces the frequency variation and the wave growth with its asymmetry in the velocity phase space.

4. Discussion

In the uniform magnetic field case, we found no triggered emission from the equatorial signal. On the other hand, in the parabolic model, a significant falling-tone emission is triggered at the termination of a short pulse with $0.51\,\Omega_e$ generated at the equator. The falling-tone emission appears in the downstream region of the triggering signal, which is contrary to the Vlasov simulation performed by (Nunn & Omura, 2012). The emission consists of a series of subpacket structures. The intense wave damping takes place at the wavefront of each packet.

To understand the generation mechanism of the emission, we analyze currents formed by energetic resonant electrons and estimate the wave growth and frequency variation via wave-particle interactions. The wave
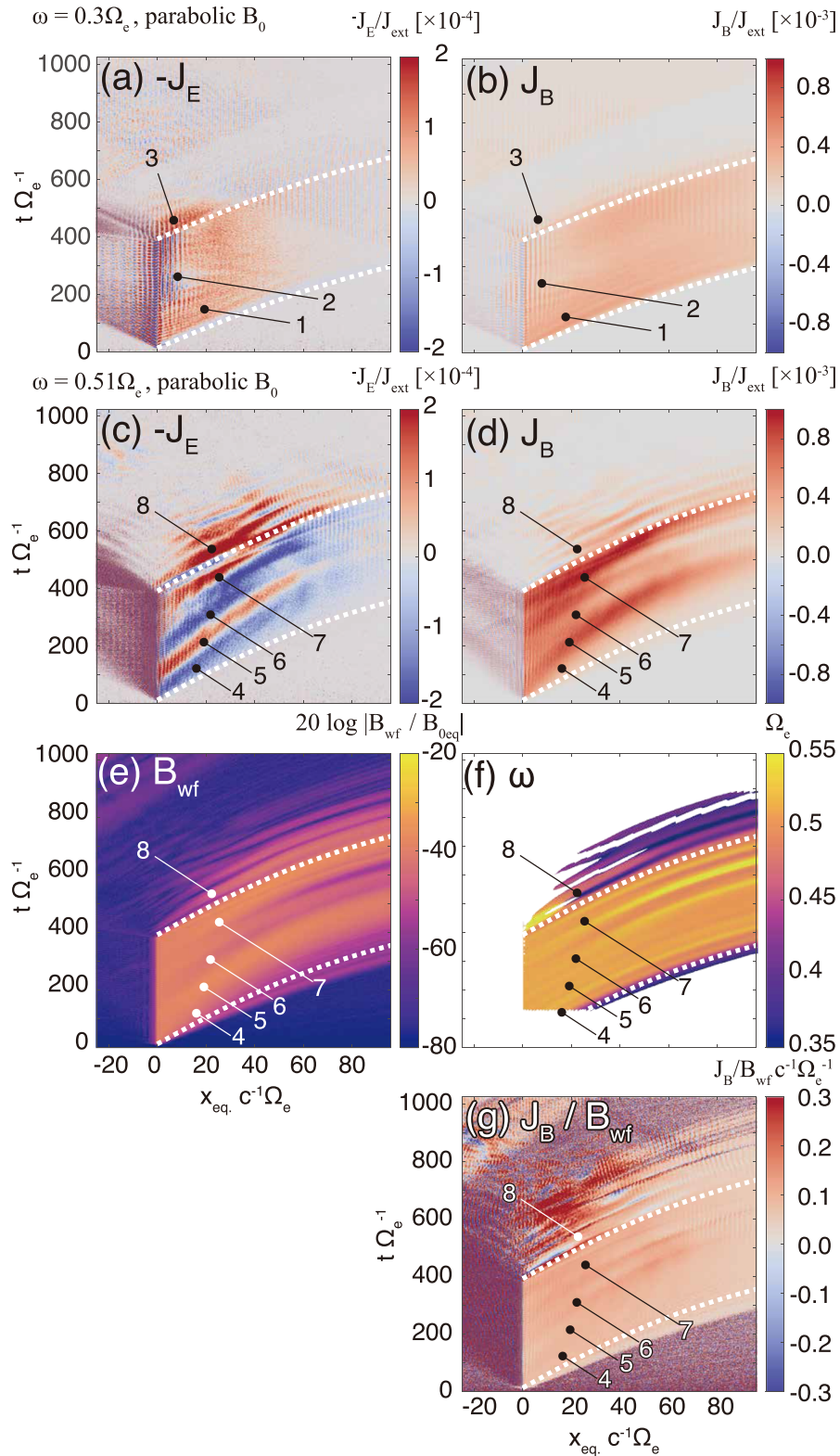
Figure 6. Spatial and temporal distribution of resonant current $-J_E$, J_B, and related field variables: (a, b) $-J_E$ and J_B for the frequency of $0.3\,\Omega_e$. (c, d) $-J_E$ and J_B for the frequency of $\omega = 0.51\,\Omega_e$. (e–g) Magnetic field amplitude for forward waves B_{wf}, instantaneous frequency ω, and J_B/B_{wf} for $\omega = 0.51\,\Omega_e$, respectively. The white dashed lines show group velocity at the frequency of the corresponding triggering frequencies using the cold plasma dispersion relation.
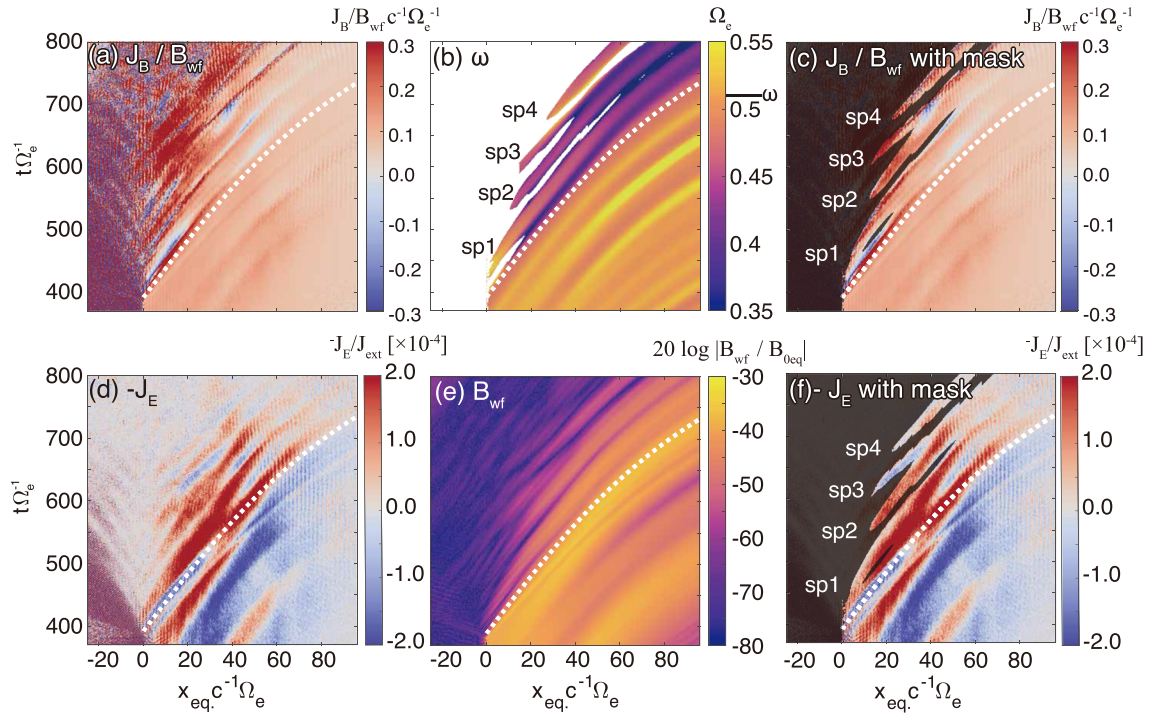
Figure 7. Falling-tone triggered wave packet from the Run 2 with the frequency of $\omega = 0.51\Omega_e$ for (a) resonant current over magnetic field of forward wave J_B/B_{fw}, (b) wave frequency ω, (c) J_B/B_{wf} for both conditions that the amplitude is more than -60 dB and that the magnitude-squared coherence at the local instantaneous frequency is more than 0.995, (d) resonant current $-J_E$, and (e) magnetic wave power $\frac{1}{2}\mu_0 B_{wf}^2$. (f) $-J_E$ by the same method as in (c).

equation and dispersion relation with resonant currents can be written as Equations 29 and 30 in Omura et al. (2008)

$$\frac{\partial B_w}{\partial t} + V_g \frac{\partial B_w}{\partial x} = -\frac{\mu_0 V_g}{2} J_E, \tag{9}$$

$$c^2 k^2 - \omega^2 - \frac{\omega \omega_{pe}^2}{\Omega_e - \omega} = \mu_0 c^2 k \frac{J_B}{B_w}, \tag{10}$$

where μ_0 is the magnetic permitivity in vacuum, J_B is the current parallel to the wave magnetic field, and J_E is the current parallel to the wave electric field, respectively. Resonant currents are formed by phase-organized electrons. Components of the resonant current parallel to the wave electric field and the wave magnetic field are defined by J_E and J_B, respectively. Omura et al. (2008) have proven that an amplitude variation is caused by J_E, and that a frequency variation is caused by J_B. The frequency variations for whistler-mode waves caused by the resonant current can be rewritten from Equation 10 as (Omura & Nunn, 2011)

$$\Delta\omega = -\frac{\mu_0 V_g}{2} \frac{J_B}{B_w}. \tag{11}$$

We calculate the spatial and temporal profiles of J_B, J_B/B_w, and J_E by interacting energetic electrons with the forward propagationg whistler-mode waves. In the simulation, we derive the resonant currents by integrating inner products between velocities of all energetic particles and forward-wave fields (i.e., $J_E = \Sigma v_\perp \cdot E_{wf}/E_{wf}$ and $J_B = \Sigma v_\perp \cdot B_{wf}/B_{wf}$). We define B_{wf} and E_{wf} as the magnetic and electric field vectors of forward propagating waves, and we denote their amplitudes by B_{wf} and E_{wf}, respectively.

We denote the characteristic areas as 1–8 in Figure 6. Negative J_E and positive J_B are formed in the triggering waves in Region 1 in Figures 6a and 6b. Although there is a weak spatial structure around Region 2,

the triggering wave of $\omega = 0.3\,\Omega_e$ result in nearly homogeneous resonant current, which causes no significant variation of the wave amplitude and the frequency.

On the other hand, Figures 6c and 6d show larger resonant currents J_E and J_B in the case of $\omega = 0.51\,\Omega_e$. We can see a sharp fluctuation of J_E changing its sign as denoted by 4–7. The stripe form of the resonant current corresponds to the group of phase bunched electrons. The emissions have an intense positive J_B, which indicates that trapped resonant electrons form an electron enhancement referred to here as the "electron hill" in the phase space. The most electrons are trapped at the wavefront of the emission and oscillate in the wave potential, which causes an oscillating sign of J_E. The intense resonant currents are caused by the greater number of resonant electrons due to the anomalous entrapping of lower pitch angle particles, which is enhanced with larger-amplitude waves with higher frequency (Kitahara & Katoh, 2019).

A remarkable feature of the falling-tone emission is intense resonant currents induced by triggering waves. These resonant currrests excite the subpacket structure with falling frequencies. Figure 7 shows enlarged views of the triggered emission. In Figures 7b, 7c, and 7f, as well as in Figure 6f, we only plot the region that satisfies the criteria described below. The enhanced resonant current J_B at the termination of the triggering pulse has a significant effect in changing the frequency because of the large J_B/B_{wf} as we find in Figures 7a and 7b. The frequency is much decreased at the termination of the triggering pulse. We calculated the coherence of the two perpendicular forward wave components B_{yf} and B_{zf}. We only plot ω, J_B/B_{wf}, and $-J_E$ of the wave packets with coherence >0.995 and wave amplitude > -60 dB of B_{eq} in Figures 7b, 7c, and 7f, respectively. We can recognize formation of subpackets as denoted by sp1, sp2, sp3, and sp4 in Figures 7b–7d.

The subpackets consist of falling-tone frequency because of the large J_B/B_{wf}, which causes the frequency decrease given by Equation 11. Omura et al. (2008) have shown that the dynamics of resonant electrons are determined by the inhomogeneity factor S. The factor is controlled by two terms containing the frequency sweep rate $\partial\omega/\partial t$ and the background magnetic field gradient $\partial B_0/\partial x$. Because of the negative frequency sweep rate $\partial\omega/\partial t < 0$, the inhomogeneity factor S becomes positive, which makes the trapped particles oscillate around the phase that gives the negative J_E as shown in Figure 7c. The negative J_E causes the growth of the subpackets as we find in Figure 7e. The sign of J_E changes depending on the sign of S. As the subpacket sp1 propagates away from the equator, the gradient of the magnetic field increases, and cancels out the contribution of the negative frequency sweep rate, and S becomes negative which makes J_E positive as shown at $x = 40\,c\Omega_e^{-1}$ and $t = 600\,\Omega_e^{-1}$ in Figure 7c. In the subpacket structure, we find a rapid variation of amplitude and instantaneous frequencies. Our results are consistent with observations reported by Shoji et al. (2018), who found rapid frequency modulation in EMIC rising-tone emissions.

5. Conclusion

We have developed a one-dimensional full PIC simulation model for studying the triggered whistler-mode emissions. We set the model so as to simulate triggered emissions from a large-amplitude wave excited artificially at the equator. With short- and large-amplitude triggering waves, falling-tone emissions consisting of several subpackets are generated in the vicinity of the magnetic equator. Each short subpacket sequentially generates the next falling-tone subpacket. We confirm that the falling tone is caused by a group of resonant electrons, forming a positive J_B/B_w, which is enhanced at the termination of the triggering waves. In the generation process of the falling tone, large variations of the amplitude B_w is essentially important for strong entrapping of resonant electrons. The resonant currents are controlled by the inhomogeneous factor S. As for the propagation process of a falling-tone subpacket, the competing relation between the negative frequency sweep rate and the positive gradient of the background magnetic field controls the sign of S and thus the convective growth of each subpacket.

In the present paper, we compare two cases of triggering frequency $0.3\,\Omega_e$ (Case 1) and $0.51\,\Omega_e$ (Case 2) to study the generation mechanisms of triggered emissions with different ranges of frequency. Based on theoretical analysis and simulation results, we conclude that a formation of the electron hill is essential for generation of falling-tone emissions. However, the different results with the two frequency ranges may not necessarily represent a general aspect of lower and upper band chorus. It is important to find general features of the excitation mechanism of upper and lower band chorus by conducting the simulation with different settings such as the frequencies and durations of the triggering pulse. In addition, the oblique

propagation of whistler-mode waves, as we find in observations, is an important physical model involving Landau resonance, which results in the amplification or damping of the waves (Hsieh & Omura, 2018). To study these effects of oblique propagations, we need to extend the current model to a two-dimensional model.

Data Availability Statement

The simulation data files and a sample program to read the data files are open to the public at the web (https://doi.org/10.5281/zenodo.3975667). The simulation data used in this paper are obtained from KEMPO1 code (https://space.rish.kyoto-u.ac.jp/software/) with minor modification including Equations 3 to 8.

References

Cornilleau-Wehrlin, N., Solomon, J., Korth, A., & Kremser, G. (1985). Experimental study of the relationship between energetic electrons and ELF waves observed on board GEOS: A support to quasi-linear theory. *Journal of Geophysical Research*, *90*(A5), 4141–4154. https://doi.org/10.1029/JA090iA05p04141

Gurnett, D. A., Huff, R. L., Pickett, J. S., Persoon, A. M., Mutel, R. L., Christopher, I. W., et al. (2001). First results from the Cluster wideband plasma wave investigation. *Annales Geophysicae*, *19*(10/12), 1259–1272. https://doi.org/10.5194/angeo-19-1259-2001

Hashimoto, K., & Kimura, I. (1981). A generation mechanism of narrow band hiss emissions above one half the electron cyclotron frequency in the outer magnetosphere. *Journal of Geophysical Research*, *86*(A13), 11,148–11,152. https://doi.org/10.1029/JA086iA13p11148

Helliwell, R. A. (1983). Controlled stimulation of VLF emissions from Siple Station, Antarctica. *Radio Science*, *18*(6), 801–814. https://doi.org/10.1029/RS018i006p00801

Helliwell, R. A. (1988). VLF wave-injection experiments from Siple Station, Antarctica. *Advances in Space Research*, *8*(1), 279–289. https://doi.org/10.1016/0273-1177(88)90373-0

Helliwell, R. A., & Brice, N. (1964). Very low frequency emission periods and whistler-mode group delays. *Journal of Geophysical Research*, *69*(21), 4704–4708. https://doi.org/10.1029/JZ069i021p04704

Helliwell, R. A., Carpenter, D. L., Inan, U. S., & Katsufrakis, J. P. (1986). Generation of band-limited VLF noise using the Siple transmitter: A model for magnetospheric hiss. *Journal of Geophysical Research*, *91*(A4), 4381–4392. https://doi.org/10.1029/JA091iA04p04381

Helliwell, R. A., Carpenter, D. L., & Miller, T. R. (1980). Power threshold for growth of coherent VLF signals in the magnetosphere. *Journal of Geophysical Research*, *85*(A7), 3360–3366. https://doi.org/10.1029/JA085iA07p03360

Helliwell, R. A., & Katsufrakis, J. P. (1974). VLF wave injection into the magnetosphere from Siple Station, Antarctica. *Journal of Geophysical Research*, *79*(16), 2511–2518. https://doi.org/10.1029/JA079i016p02511

Hikishima, M., Omura, Y., & Summers, D. (2010). Self-consistent particle simulation of whistler mode triggered emissions. *Journal of Geophysical Research*, *115*, A12246. https://doi.org/10.1029/2010JA015860

Hsieh, Y.-K., & Omura, Y. (2018). Nonlinear damping of oblique whistler mode waves via Landau resonance. *Journal of Geophysical Research: Space Physics*, *123*, 7462–7472. https://doi.org/10.1029/2018JA025848

Katoh, Y., & Omura, Y. (2007). Computer simulation of chorus wave generation in the Earth's inner magnetosphere. *Geophysical Research Letters*, *34*, L03102. https://doi.org/10.1029/2006GL028594

Ke, Y., Gao, X., Lu, Q., Wang, X., & Wang, S. (2017). Generation of rising-tone chorus in a two-dimensional mirror field by using the general curvilinear PIC code. *Journal of Geophysical Research: Space Physics*, *122*, 8154–8165. https://doi.org/10.1002/2017JA024178

Kennel, C. F., & Petschek, H. E. (1966). Limit on stably trapped particle fluxes. *Journal of Geophysical Research*, *71*(1), 1–28. https://doi.org/10.1029/JZ071i001p00001

Kitahara, M., & Katoh, Y. (2019). Anomalous trapping of low pitch angle electrons by coherent whistler mode waves. *Journal of Geophysical Research: Space Physics*, *124*, 5568–5583. https://doi.org/10.1029/2019JA026493

Koons, H. C., & Roeder, J. L. (1990). A survey of equatorial magnetospheric wave activity between 5 and 8 R_E. *Planetary and Space Science*, *38*(10), 1335–1341. https://doi.org/10.1016/0032-0633(90)90136-E

LeDocq, M. J., Gurnett, D. A., & Hospodarsky, G. B. (1998). Chorus source locations from VLF poynting flux measurements with the polar spacecraft. *Geophysical Research Letters*, *25*(21), 4063–4066. https://doi.org/10.1029/1998GL900071

Lu, Q., Ke, Y., Wang, X., Liu, K., Gao, X., Chen, L., & Wang, S. (2019). Two-dimensional gcPIC simulation of rising-tone chorus waves in a dipole magnetic field. *Journal of Geophysical Research: Space Physics*, *124*, 4157–4167. https://doi.org/10.1029/2019JA026586

Meredith, N. P., Horne, R. B., & Anderson, R. R. (2001). Substorm dependence of chorus amplitudes: Implications for the acceleration of electrons to relativistic energies. *Journal of Geophysical Research*, *106*(A7), 13,165–13,178. https://doi.org/10.1029/2000JA900156

Nunn, D. (1974). A self-consistent theory of triggered VLF emissions. *Planetary and Space Science*, *22*(3), 349–378. https://doi.org/10.1016/0032-0633(74)90070-1

Nunn, D. (1986). A nonlinear theory of sideband stability in ducted whistler mode waves. *Planetary and Space Science*, *34*(5), 429–451. https://doi.org/10.1016/0032-0633(86)90032-2

Nunn, D. (1990). The numerical simulation of VLF nonlinear wave-particle interactions in collision-free plasmas using the Vlasov hybrid simulation technique. *Computer Physics Communications*, *60*(1), 1–25. https://doi.org/10.1016/0010-4655(90)90074-B

Nunn, D., & Omura, Y. (2012). A computational and theoretical analysis of falling frequency VLF emissions. *Journal of Geophysical Research*, *117*, A08228. https://doi.org/10.1029/2012JA017557

Nunn, D., Omura, Y., Matsumoto, H., Nagano, I., & Yagitani, S. (1997). The numerical simulation of VLF chorus and discrete emissions observed on the geotail satellite using a Vlasov code. *Journal of Geophysical Research*, *102*(A12), 27,083–27,097. https://doi.org/10.1029/97JA02518

Nunn, D., Santolík, O., Rycroft, M., & Trakhtengerts, V. (2009). On the numerical modelling of VLF chorus dynamical spectra. *Annales Geophysicae*, *27*(6), 2341–2359. https://doi.org/10.5194/angeo-27-2341-2009

Oliven, M. N., & Gurnett, D. A. (1968). Microburst phenomena: 3. an association between microbursts and VLF chorus. *Journal of Geophysical Research*, *73*(7), 2355–2362. https://doi.org/10.1029/JA073i007p02355

Omura, Y. (2007). One-dimensional electromagnetic particle code KEMPO1: A tutorial on microphysics in space plasmas. In H. Usui & Y. Omura (Eds.), *Advanced methods for space simulations* (pp. 1–21). Tokyo: Terra Scientific Publishing Company.

Omura, Y., Hikishima, M., Katoh, Y., Summers, D., & Yagitani, S. (2009). Nonlinear mechanisms of lower-band and upper-band VLF chorus emissions in the magnetosphere. *Journal of Geophysical Research*, *114*, A07217. https://doi.org/10.1029/2009JA014206

Omura, Y., Katoh, Y., & Summers, D. (2008). Theory and simulation of the generation of whistler-mode chorus. *Journal of Geophysical Research*, *113*, A04223. https://doi.org/10.1029/2007JA012622

Omura, Y., & Matsumoto, H. (1993). KEMPO1: Technical guide to one-dimensional electromagnetic particle code. In H. Matsumoto & Y. Omura (Eds.), *Computer space plasma physics: Simulation techniques and softwares* (pp. 21–65). Tokyo: Terra Scientific Publishing Company.

Omura, Y., & Nunn, D. (2011). Triggering process of whistler mode chorus emissions in the magnetosphere. *Journal of Geophysical Research*, *116*, A05205. https://doi.org/10.1029/2010JA016280

Parrot, M., Santolík, O., Cornilleau-Wehrlin, N., Maksimovic, M., & Harvey, C. C. (2003). Source location of chorus emissions observed by Cluster. *Annales Geophysicae*, *21*(2), 473–480. https://doi.org/10.5194/angeo-21-473-2003

Santolík, O., Gurnett, D. A., & Pickett, J. S. (2004). Multipoint investigation of the source region of storm-time chorus. *Annales Geophysicae*, *22*(7), 2555–2563. https://doi.org/10.5194/angeo-22-2555-2004

Santolík, O., Gurnett, D. A., Pickett, J. S., Parrot, M., & Cornilleau-Wehrlin, N. (2005). Central position of the source region of storm-time chorus. *Planetary and Space Science*, *53*(1), 299–305. https://doi.org/10.1016/j.pss.2004.09.056

Santolík, O., Macusova, E., Titova, E. E., Kozelov, B. V., Gurnett, D. A., Pickett, J. S., et al. (2008). Frequencies of wave packets of whistler-mode chorus inside its source region: A case study. *Annales Geophysicae*, *26*(6), 1665–1670. https://doi.org/10.5194/angeo-26-1665-2008

Shoji, M., Miyoshi, Y., Omura, Y., Kistler, L. M., Kasaba, Y., Matsuda, S., et al. (2018). Instantaneous frequency analysis on nonlinear EMIC emissions: Arase observation. *Geophysical Research Letters*, *45*, 13,199–13,205. https://doi.org/10.1029/2018GL079765

Solomon, J., Cornilleau-Wehrlin, N., Korth, A., & Kremser, G. (1988). An experimental study of ELF/VLF hiss generation in the Earth's magnetosphere. *Journal of Geophysical Research*, *93*(A3), 1839–1847. https://doi.org/10.1029/JA093iA03p01839

Tao, X. (2014). A numerical study of chorus generation and the related variation of wave intensity using the DAWN code. *Journal of Geophysical Research: Space Physics*, *119*, 3362–3372. https://doi.org/10.1002/2014JA019820

Trakhtengerts, V. Y., Rycroft, M. J., & Demekhov, A. G. (1996). Interrelation of noise-like and discrete ELF/VLF emissions generated by cyclotron interactions. *Journal of Geophysical Research*, *101*(A6), 13,293–13,301. https://doi.org/10.1029/95JA03515

Tsurutani, B. T., & Smith, E. J. (1974). Postmidnight chorus: A substorm phenomenon. *Journal of Geophysical Research*, *79*(1), 118–127. https://doi.org/10.1029/JA079i001p00118

Tsurutani, B. T., Smith, E. J., West, H. I., & Buck, R. M. (1979). Chorus, energetic electrons and magnetospheric substorms. In P. J. Palmadesso, & K. Papadopoulos (Eds.), *Wave instabilities in space plasmas* (pp. 55–62). Dordrecht: Springer Netherlands.

Umeda, T., Omura, Y., & Matsumoto, H. (2001). An improved masking method for absorbing boundaries in electromagnetic particle simulations. *Computer Physics Communications*, *137*(2), 286–299. https://doi.org/10.1016/S0010-4655(01)00182-5